FULL TITLE:

End-to-end multimodal 3D imaging and machine learning workflow for non-destructive diagnosis of vine trunk diseases

AUTHORS

Romain Fernandez[1,2,10]*, Loïc Le Cunff[1,10], Samuel Mérigeaud[3], Jean-Luc Verdeil[4,10], Julie Perry[5], Philippe Larignon[6], Anne-Sophie Spilmont[7], Philippe Chatelet[10], Maïda Cardoso[8], Christophe Goze-Bac[9], and Cédric Moisy[1,10]*

AFFILIATIONS

[1] IFV, French Institute of Vine and Wine, UMT Géno-Vigne, IFV, INRAE, Institut Agro, F-34398 Montpellier, France.
[2] CIRAD, UMR AGAP Institut, F-34398 Montpellier, France.
[3] TRIDILOGY SARL, Groupe CRP - VIDI, Montpellier, France.
[4] CIRAD, Phiv, Campus Lavalette, 389 Avenue Agropolis, Montferrier-sur-Lez, France.
[5] CIVC Comité Champagne, 5 rue Henri Martin, 51200 Epernay, France.
[6] IFV Nîmes. Pôle Rhône-Méditerranée, 7 avenue Cazeaux, 30230 Rodilhan, France
[7] IFV Pôle Matériel Végétal, Domaine de l'Espiguette, 30240 Le Grau du Roi, France.
[8] BNIF University of Montpellier, Place Eugène Bataillon, Montpellier, France.
[9] Laboratoire Charles Coulomb, University of Montpellier and CNRS, 34095 Montpellier, France
[10] UMR AGAP Institut, Univ Montpellier, CIRAD, INRAE, Institut Agro, Montpellier, France.
* These authors contributed equally to this work.

Corresponding author:
Cédric Moisy
Email: cedric.moisy@vignevin.com
Tel: +33(0)467614471

ABSTRACT

Worldwide, vineyards sustainability is threatened by grapevine (*Vitis vinifera* L.) trunk diseases (GTD), which spread insidiously, irreversibly degrading internal trunk tissues and ultimately entailing vine death. Foliar symptoms can erratically appear, but the sanitary status of vines cannot be ascertained without injuring the plants. To tackle this challenge, we developed a novel approach based on multimodal 4D imaging and artificial intelligence (AI)-based image processing that allowed a non-invasive GTD diagnosis. Each imaging modality contribution to tissue discrimination was evaluated, and we identified quantitative structural and physiological markers characterizing wood degradation. The combined study of the anatomical distribution of degraded tissues and the foliar symptom history of plants collected in a vineyard in Champagne, France, demonstrated that white rot and intact tissue contents were key measurements. We finally proposed a model for an accurate GTD diagnosis. This work opens new routes for precision agriculture by permitting field monitoring of GTD and surveying plant health *in situ*.

KEY WORDS

3D imaging; image processing; MRI; Fungal pathogens; Plant diseases; *Vitis vinifera L.* (grapevine); Wood; X-ray CT

INTRODUCTION

Grapevine trunk diseases (GTDs) are a major cause of vine decline worldwide (1). They are mostly undetectable until advanced stages are reached, and the European Union has banned the only effective treatment, i.e., an arsenic-based pesticide. Therefore, vineyards sustainability is jeopardized, with yearly losses up to several billion dollars (2, 3).

GTDs detection and monitoring are extremely challenging: fungal pathogens insidiously colonize trunks, leaving different types of irreversibly decayed tissues (1). The predominant GTD, Esca dieback, induces typical tiger stripe-like foliar symptoms observed erratically, but their origin remains poorly understood (4) and their sole observation is not indicative of the vines' sanitary status (5-8). Quantifying degraded tissues within living vines could help determine the plant condition and predict disease evolution, but classical techniques (9) require sacrificing the plant, often yielding limited information. Reaching a reliable diagnosis is thus impossible in living plants.

To address this issue, we developed a novel approach based on medical multimodal imaging (Magnetic Resonance Imaging (MRI) and X-ray computed tomography (CT)) and assisted by AI-based automatic segmentation that allows unprecedented non-invasive diagnosis of GTDs. We were able to perform an accurate detection and quantification of healthy and unhealthy wood compartments within twelve entire vines from a vineyard in Champagne, France. As in medicine (10), vine-specific "digital twins" could revolutionize viticulture by providing diseased vines-dedicated models, and computerized assistance to diagnosis.

We identified structural and physiological markers characterizing the early and late stages of wood degradation and assessed the contribution and efficiency of each imaging technique to their detection. We finally studied the relationships between foliar symptoms and the anatomical distribution of intact, degraded, and white rot tissues. This study gives access to key indicators of the vine sanitary status and enables solutions for field monitoring of GTDs and other complex diseases.

RESULTS

Multimodal 3D imaging of healthy and sick tissues in vines

Based on foliar symptom history, *symptomatic*- and *asymptomatic*-looking vines (twelve total) were collected in 2019 from a Champagne vineyard (France) and imaged using four different modalities: X-ray CT and a combination of multiple MRI protocols: T1-, T2-, and PD-weighted (w) (Fig. 1). Following imaging acquisitions, vines were molded, sliced, and each side of the cross-sections photographed (approx. 120 pictures per plant). Eighty-four random cross-sections and their corresponding images were manually annotated by experts according to visual inspection of tissue appearance. Six classes showing specific colorations were defined (Fig. 2.a): (i) healthy-looking tissues showing no sign of degradation; and unhealthy-looking tissues such as (ii) black punctuations, (iii) reaction zones, (iv) dry tissues, (v) necrosis associated with GTD (incl. Esca and Eutypa dieback), and (vi) white rot (decay). The 3D data resulting from each imaging modality (three MRI, X-ray CT, and registered photographs) were aligned into 4D-multimodal images (11). It enabled 3D voxel-wise joint exploration of the modality's information and its confrontation with ground-truth annotations by experts (Fig. 2.b).

A preliminary study of manually annotated random cross-sections led to the identification of general signal trends distinguishing healthy- and unhealthy-looking tissues (Fig. 2.a, 2.c and 2.d).

Considering healthy-looking wood, areas of functional tissues were associated with high X-ray absorbance and high MRI values (i.e., high NMR signals in T1-, T2-, and PD-weighted images) while non-functional wood showed slightly lower X-ray absorbance (approx. -10%) and lower values in all three MRI modalities (-30 to -60%).

As to unhealthy-looking tissues, signals were highly variable. Dry tissues, resulting from wounds inflicted during seasonal pruning, exhibited medium X-ray absorbance and very low MRI values in all three modalities. Necrotic tissues, corresponding to different types of GTD necrosis, showed medium X-ray absorbance (approx. -30% compared to functional tissues) and medium to low values in T1-w images, while signals in T2-w and PD-w were close to zero (-60 to -85%). Black punctuations, known as clogged vessels, generally colonized by the fungal pathogen *Phaeomoniella chlamydospora*, were characterized by high X-ray absorbance, medium values in T1-w, and variable values in T2-w and PD-w. Finally, *white rot*, the most advanced stage of degradation, exhibited significantly lower mean values in X-ray absorbance (-70% compared to functional tissues; -50% compared to necrotic ones) and in MRI modalities (-70 to -98%).

Interestingly, some regions of healthy-looking (uncolored) tissues showed a particularly strong hypersignal in T2-w compared to the surrounding ones (Fig. 2.d). Located in the vicinity of necrotic tissue boundaries and sometimes undetectable by visual inspection of the wood, these regions most probably corresponded to reaction zones described earlier as areas where host and pathogens strongly interact and showing specific MRI signatures (12).

These results highlighted the benefits of multimodal imaging in distinguishing different

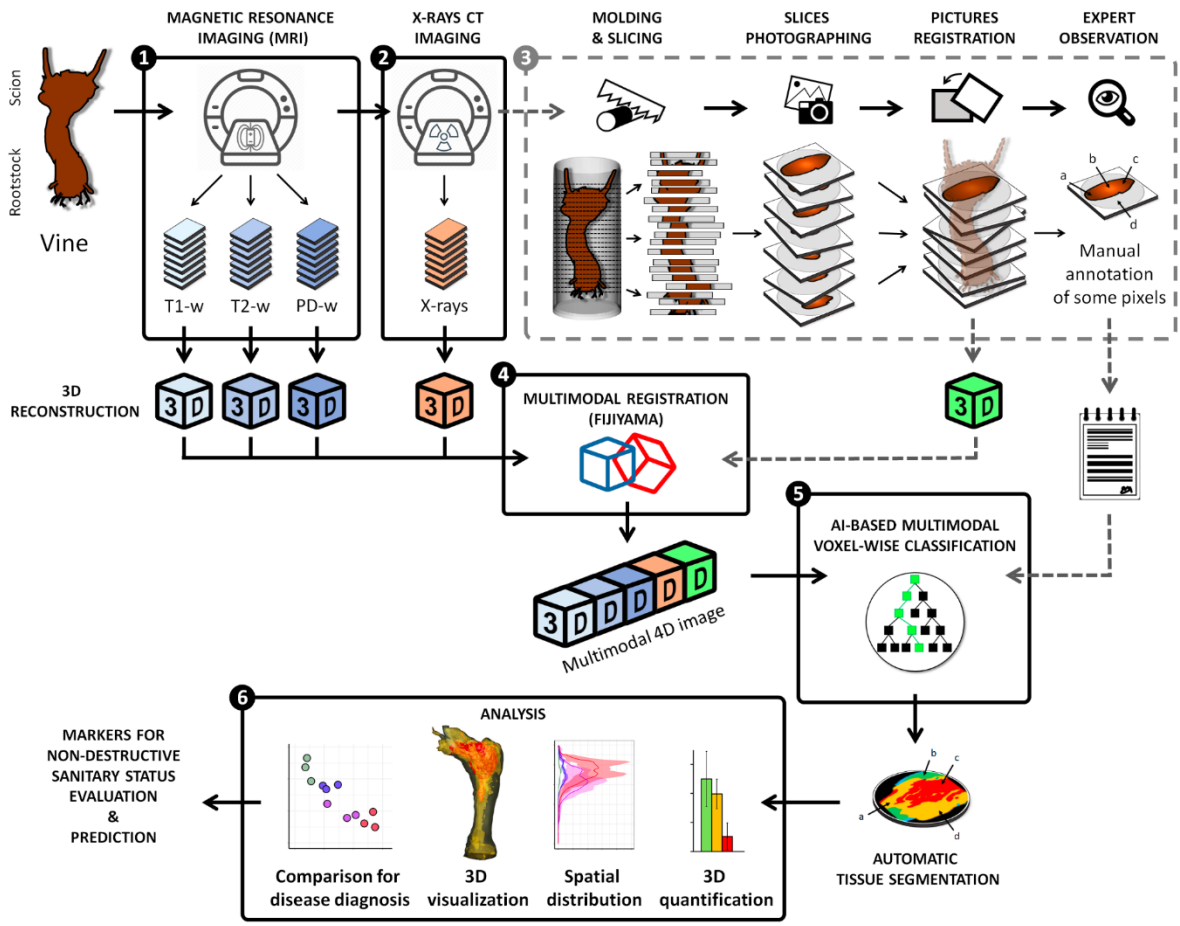

Figure 1

tissues for their degree of degradation, and in characterizing signatures of the degradation process. The loss of function was properly highlighted by a significant MRI hypo signal. The necrosis-to-decay transition was marked by a strong degradation of the tissue structure and a loss of density revealed by a reduction in X-ray absorbance. While distinguishing different types of necrosis remained challenging because their signal distributions overlap, degraded tissues exhibited multimodal signatures permitting their detection. Interestingly, specific events such as reaction zones were detected by combining X-ray and T2-w modalities. Overall, MRI appeared to be better suited for assessing functionality and investigating physiological phenomena occurring at the onset of wood degradation when the wood still appeared healthy (Fig. 2.f). On the opposite, X-ray CT seemed more suited for the discrimination of more advanced stages of degradation.

Figure 1: General Workflow: from wine multimodal imaging to data analysis.

(1) and (2) Multimodal 3D imaging of a vine using MRI (T1-weighted, T2-w, and PD-w) and X-ray CT.

(3) (Optional step) the vine is molded and then sliced every 6 mm. Pictures of cross-sections (both sides) are registered in a 3D photographic volume and some cross-sections are manually annotated by experts.

(4) Multimodal registration of the MRI, X-ray CT, and photographic data into a coherent 4D image using Fijiyama (11).

(5) Machine-learning based voxel classification. Segmentation of images based on the tissue expert manual annotations: wood (*intact*, *degraded*, *white rot*), *bark* and *background*. The classifier was trained and evaluated using manual annotations collected on different vines during step 3.

(6) Data analysis and visualization.

Automatic segmentation of *intact*, *degraded*, and *white rot* tissues using non-destructive imaging

To propose a proper *in vivo* GTD diagnosis method, we aimed to assess vines' condition by quantifying automatically and non-destructively the trunks' healthy and unhealthy inner compartments in 3D. To achieve this complex task, we trained a segmentation model to detect the level of degradation voxel-wise, using imaging data acquired with non-destructive devices. We defined three main classes corresponding to the level of tissue degradation: (1) "*intact*" for functional or non-functional but healthy tissues; (2) "*degraded*" for necrotic and other altered tissues; and (3) "*white rot*" for decayed wood (Fig. 2.a).

An algorithm was trained to automatically classify each voxel in one of the three classes, based on its T1-w, T2-w, PD-w, and X-ray absorbance values (Fig. 3.a). The classification was performed using the Fast Random Forest algorithm implemented in the Weka library (13). The algorithm was first trained on a set of 81,454 manually annotated voxels (Table S1), then cross-validated, and finally applied to whole 4D-images (46.2 million voxels total) (Fig. 1.4). The mean global accuracy of the classifier (91.6% ± 2.0) indicated a high recognition rate, with minor variations among cross-validation folds (Table S2). In our evaluation, F1 scores were 93.6% (± 3.7) for *intact*, 90.0% (± 3.8) for *degraded*, and 91.4% (± 6.8) for *white rot* tissue classes. The global confusion matrix of the validation sets, summed over the 66 folds (895,994 samples), showed that the great majority of incorrect classifications were either due to confusions between *intact* and *degraded* classes (53.4%) or between *degraded* and *white rot* (20.8%) (Table S3). *Intact* and *white rot* classes were almost never confused (<0.001% error).

The same validation protocol was used to compare the effectiveness of all possible

combinations of imaging modalities for tissue detection (Fig. 3.b): the most efficient combination was [T1-w, T2-w, X-ray] for detection of *intact* (F1= 93.9% ± 3.4) and *degraded* tissues (90.5% ± 3.2); and [T1-w, X-ray] for *white rot* (93.0% ± 5.1). Interestingly, the X-ray modality considered alone reached almost similar scores for *white rot* detection. In general, slightly better results (± 0.5%) were obtained without considering the PD-w modality, most probably due to its lower initial resolution.

The classifier was finally applied to the whole dataset, and statistics were computed to compare the tissue contents in different vines. Considering the entire classified dataset (46.2 million voxels), mean signal values significantly declined between *intact* and *degraded* tissues (-19.3% for X-ray absorbance; and -57.3%, -86.3% and -71.3% for MRI T1-w, T2-w, and PD-w, respectively); and between *degraded* and *white rot* (-56.0% for X-ray absorbance; and -36.8%, -76.8% and -64.2% for MRI T1-w, T2-w, and PD-w, respectively) (Fig. 2.e and Table S4).

With the increasing deployment of X-ray and NMR devices on phenotyping tasks, in-field

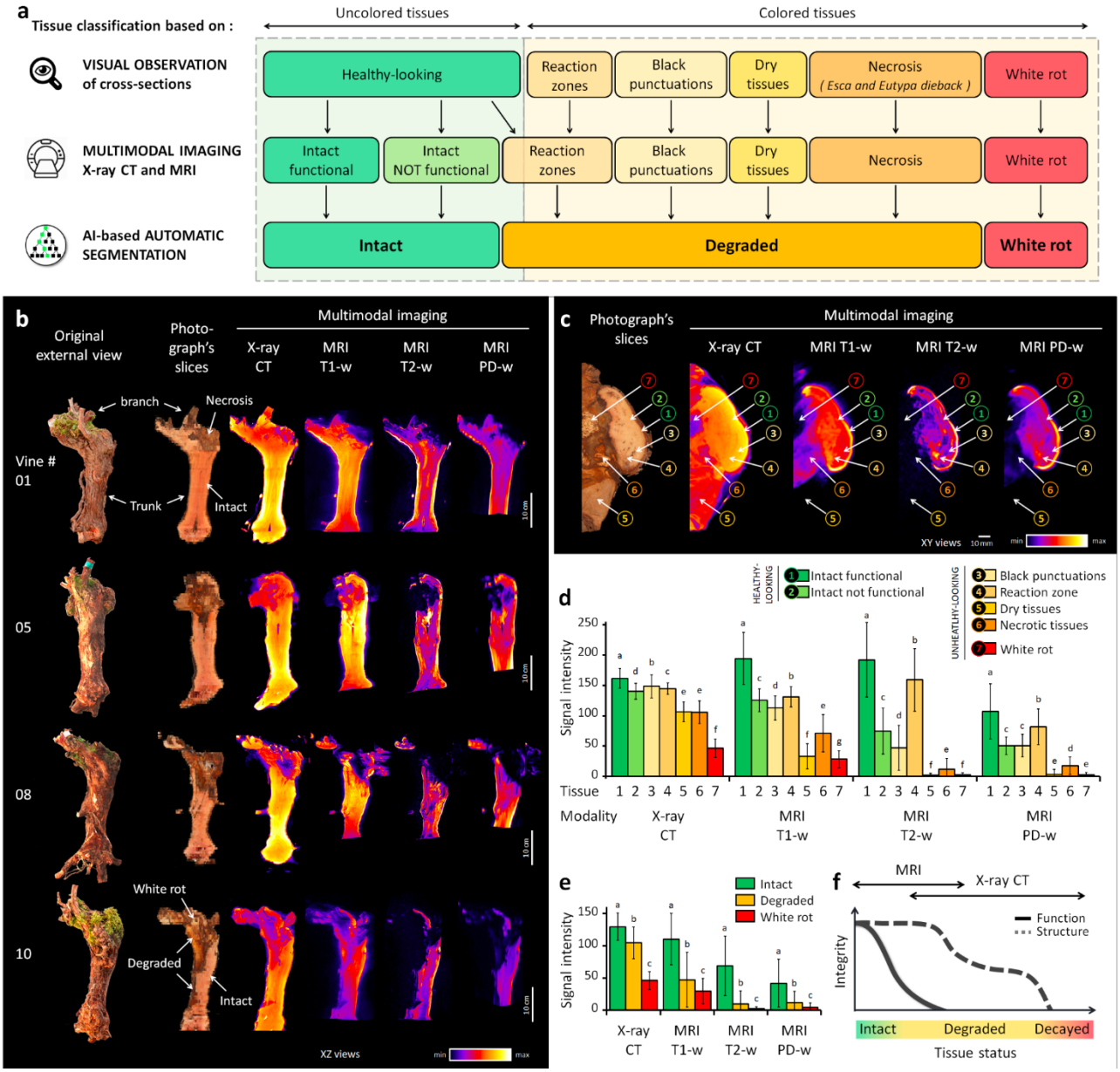

Figure 2

imaging has become accessible, but at a heavy cost in terms of image quality and resolution. We challenged our method by training and evaluating the classifier at coarser resolutions, ranging from 0.7 up to 10 mm per voxel (Fig. 3.c). Results proved our approach maintained correct performances even at 10 mm (F1 ≥ 80% for *I*; ≥ 70% for *D* and *WR*) while a human operator is no longer able to recognize any anatomical structure or tissue class at this resolution.

These results confirmed both the wide range of potential applications and the complementarity of the four imaging modalities. Combining medical imaging techniques and an AI-based classifier, it was possible to segment intact, degraded, and white rot compartments automatically and non-destructively inside the wood. This represents an important breakthrough in their visualization, volumic quantification and localization in the entire 3D volume of the vines (Fig. 3.d).

Figure 2: Multimodal imaging and signal analysis.

a) Comparison of tissue classification based either on visual observation of trunk cross-sections (6 classes), multimodal imaging data (7 classes), or AI-based segmentation (3 classes).

b) Multimodal imaging data collected on vines. XZ views of the photographic, X-ray CT, and MRI volumes, after registration using Fijiyama (11).

c) Example of manual tissue annotation and corresponding multimodal signals.

d) Multimodal signal values collected by manual annotation of tissues on random trunk cross-sections (19,372 voxels total).

e) Multimodal signal values collected automatically on all 4D datasets (46.2 million voxels total) after AI-based voxel classification in three main tissue classes defined as *Intact*, *Degraded* and *White rot*.

f) General trends for functional and structural properties during the wood degradation process, and proposed fields of application for MRI and X-ray CT imaging.

Legend: letters on bar plots correspond to Tukey tests for the comparison of tissue classes in each modality.

Deciphering the relationship between inner tissue composition and external symptomatic histories: a step forward toward a reliable *in situ* diagnosis

Non-destructive detection of GTDs in vineyards is currently only possible through the observation of foliar symptoms and vine mortality, and numerous studies are based on these proxies for phenotyping. Foliage is usually screened at specific periods of the year when Esca or Eutypa dieback symptoms occur, and this screening is usually repeated for one or several years. New leaves are produced each year and symptoms may not recur in following years, making any diagnosis hazardous at best, and attempts to correlate external and internal impacts of GTDs unsuccessful. Here, foliar symptoms were recorded each year for twenty years, i.e., since the plot was planted in 1999 (Fig. 4.a). Together with the accurate quantification and localization of degraded and non-degraded compartments in trunks, this allowed more advanced investigations.

Using only foliar symptoms observed in 2019 as markers, half of the vines would have been misclassified as "*healthy*" plants although harboring significantly degraded internal tissues (Fig. 4.b). Indeed, despite the absence of leaf symptoms these vines contained important volumes of deteriorated wood (up to 623 cm^3 of *degraded* tissues and 281 cm^3 of *white rot*) (Table S5). Considering one year at a time, the foliar symptom proxy would have led to different -and erroneous- diagnoses each year, confirming its

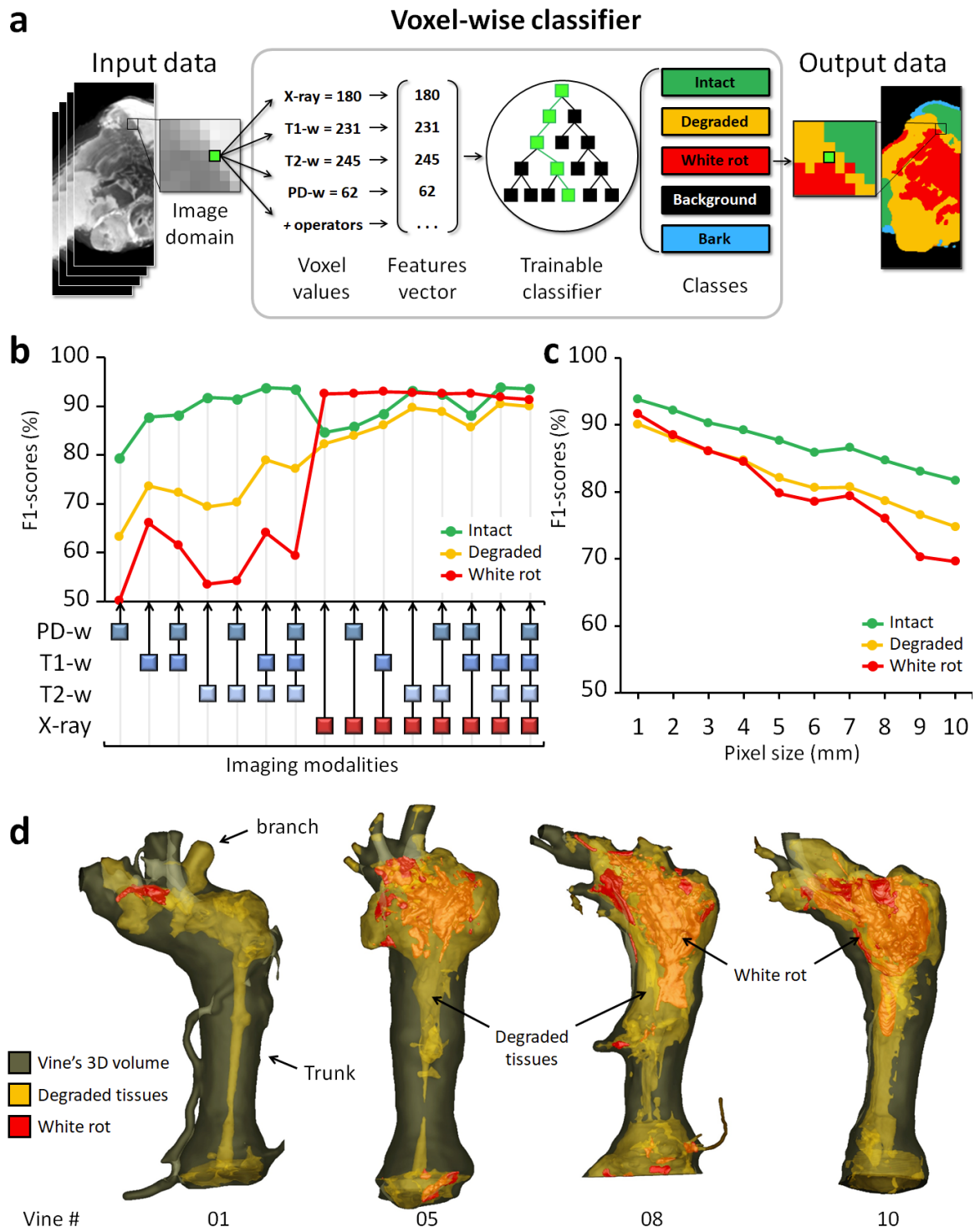

Figure 3

unreliability (Fig. 4.a). Correlations between foliar symptoms observed in 2019 and total internal contents were indeed very weak (R^2= -0.25, 0.27 and 0.18 for *intact*, *degraded*, and *white rot*, respectively). On the opposite, internal tissue contents were better supported by categories considering the complete vine history (Fig. 4.c). For example, the sum of foliar symptoms detected during the vine's life was strongly correlated to the composition of internal tissues (R^2= -0.87, 0.79, and 0.84 for *intact*, *degraded*, and *white rot*, respectively) and the correlation

between inner contents and the date of the first foliar symptom expression was also high (-0.87 for *intact*, 0.91 for *white rot*) (Table S6).

As illustrated by 3D reconstructions (Fig. 3.d), *degraded* and *white rot* compartments were mostly continuous and located in the top of the vine trunk. This result was consistent with previous reports and the positioning of most pruning injuries that are considered as pathways for the penetration of fungal pathogens causing GTDs (1). However, the distribution and volumes of the three tissue classes helped distinguish different degrees in disease severity (Fig. 4.d). In detail, the tissue content located in the upper last centimeters of the trunk and the insertion point of branches allowed efficient discrimination of the vine condition (Fig. 4.e). On one hand, the proportion of *intact* tissues detected in this region discriminated between vines with mild forms of the disease (*intact* > 30%) and vines at more advanced stages (< 30%). On the other hand, the proportion of *white rot* distinguished the healthiest vines (*white rot* < 8%), more affected ones (8 to 15%), and the ones facing critical stages (> 15%). The volume of *degraded* tissues, together with the positioning of *intact* and *white rot* tissues, allowed to fine-tune the diagnosis (Fig. S1).

Non-invasive imaging and 3D modeling offered the possibility to access both internal tissue contents and spatial information without harming the plant (Fig. 5). In vines suffering from advanced stages of trunk diseases, *white rot* tissues were surrounded by *degraded* tissues, while only thin areas of *intact* functional tissues were limited to the periphery of trunk tops. As illustrated in Fig. 5, abiotic stresses such as a fresh wound can also have a huge impact on the functionality of surrounding tissues and affect even more plant survival.

Figure 3: Automatic tissues segmentation

a) AI-based image segmentation using multimodal signals.

b) Comparison of all possible imaging modality combinations for their effectiveness (F1-scores) in tissue detection.

c) Effectiveness of tissue detection at lower imaging resolutions (using four modalities).

d) 3D reconstructions highlighting the extent and localization of the *degraded* and *white rot* compartments in four vines.

Figure 4: Deciphering the relationship between inner tissue degradation and external foliar symptoms.

a) Left: Detailed history of external GTD symptoms expression. Right: classification of vines based on their external sanitary status, either considering year 2019 only or the complete symptom history (right).

b) and c) Internal tissue contents of the trunks. Vines are grouped per phenotypic categories, based either on the single 2019 observation or the complete 1999-2019 symptom history.

Tissue percentages are calculated from the upper 25 cm of the trunk.

d) Comparison of phenotypic categories for the *white rot* and *intact* tissues distribution (mean and interval) along the trunk. Position 0 cm corresponds to the top of the trunk and initiation of branches (i.e., > 0 in branches; < 0 in trunk).

e) Comparison of vines for *intact* and *white rot* tissue contents in the region -2 to +2 cm (last 2cm of the trunk and first 2 cm of the branches).

Figure 5: 3D visualization of internal tissue contents: example of a specimen at the critical stage of vine decline

a) Original external view of the vine.

b) Combining MRI data volume rendering and white rot model.

c) 3D representation of the *intact (green)*, *degraded (orange)* and *white rot* (red) compartments inside the trunk.

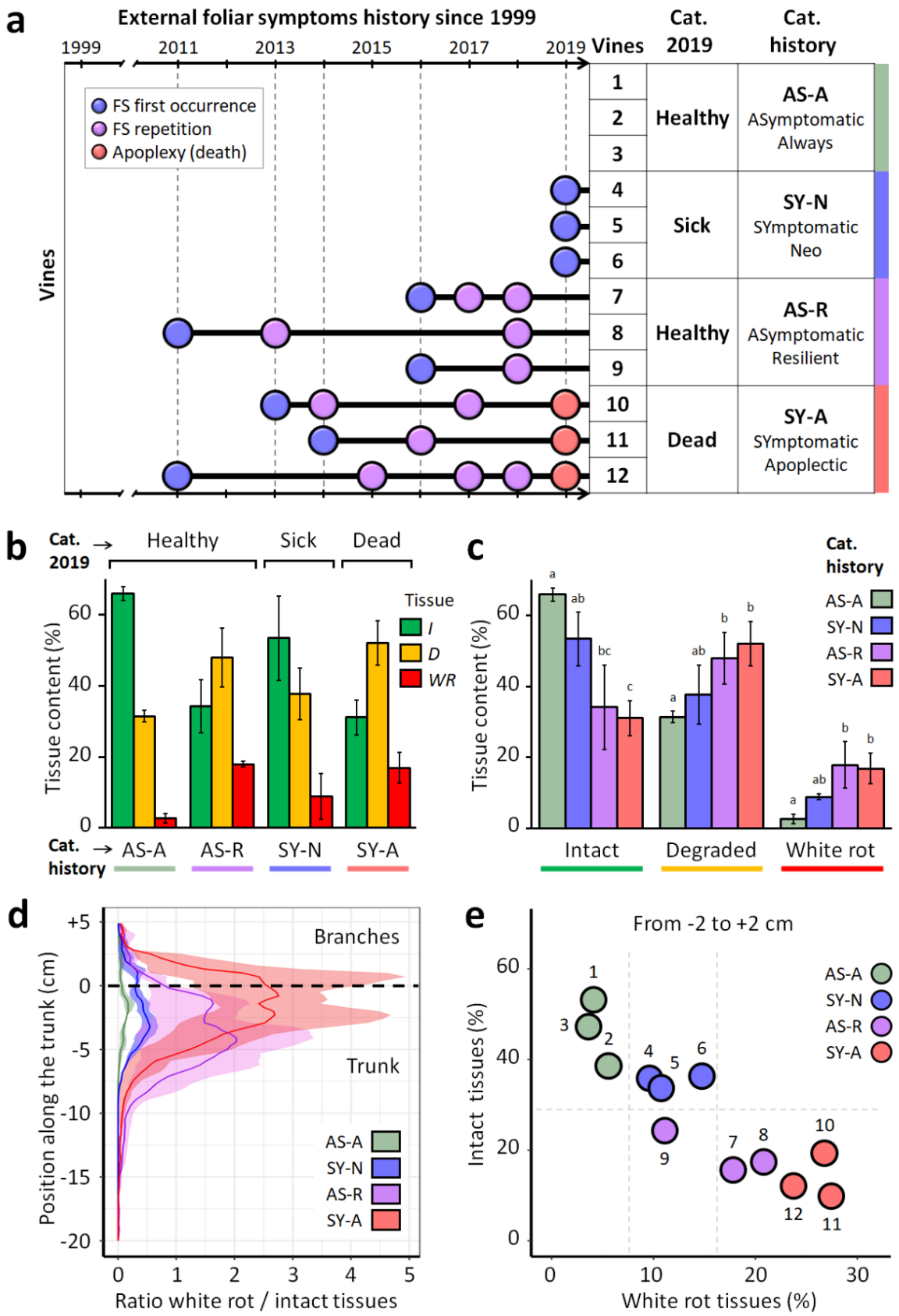
a
External foliar symptoms history since 1999
1999
2011
2013
2015
2017
2019
Vines
Cat. 2019
Cat. history
FS first occurrence
FS repetition
Apoplexy (death)
Vines
1
2
3
4
5
6
7
8
9
10
11
12
Healthy
Sick
Healthy
Dead
AS-A
ASymptomatic
Always
SY-N
SYmptomatic
Neo
AS-R
ASymptomatic
Resilient
SY-A
SYmptomatic
Apoplectic
b
Cat. 2019
Healthy
Sick
Dead
Tissue
I
D
WR
Tissue content (%)
Cat. history
AS-A
AS-R
SY-N
SY-A
c
Cat. history
AS-A
SY-N
AS-R
SY-A
Tissue content (%)
Intact
Degraded
White rot
d
Branches
Trunk
Position along the trunk (cm)
Ratio white rot / intact tissues
e
From -2 to +2 cm
Intact tissues (%)
White rot tissues (%)

Figure 4

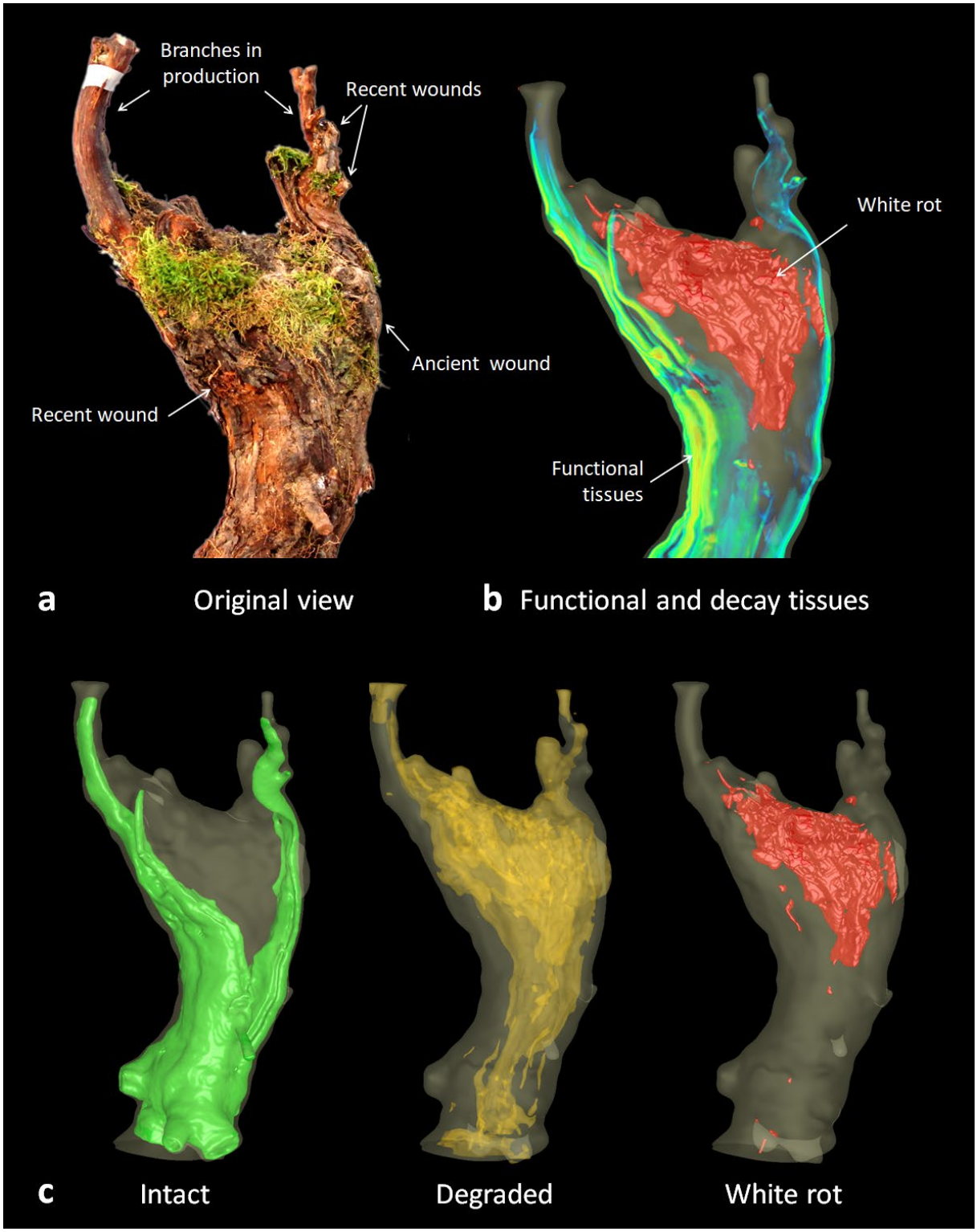
Branches in production
Recent wounds
Ancient wound
Recent wound
a
Original view
White rot
Functional tissues
b
Functional and decay tissues
c
Intact
Degraded
White rot

Figure 5

DISCUSSION

A new method for non-destructive detection of wood diseases

GTDs are mostly undetectable until advanced stages are reached, and their detection is currently only possible through destructive techniques or the observation of erratically expressed foliar symptoms. A non-destructive and reliable method for detecting GTDs is frequently expected (1, 14-16). To that end, we developed an innovative approach to non-destructively measure healthy and unhealthy tissues in living perennial vines. We combined 1) non-invasive 3D imaging techniques originated from the medical field; 2) a registration pipeline for multimodal data; and 3) a machine-learning based model for voxel classification. We were able to determine voxel-wise the level of tissue degradation, and to accurately segment, visualize, and quantify healthy and unhealthy compartments in the plants.

Among the imaging modalities tested, MRI already proved relevant to assess tissue functions in grapevine (17) and in several applications in living plants (18). In a recent study, MRI surprisingly failed to distinguish healthy and necrotic tissues in grapevine trunk samples (19). Here MRI was found particularly well suited for detecting early stages of wood degradation, characterized by a significant loss of signal (57 to 86%) in T1-w and T2-w protocols between *intact* and *degraded* tissue classes. Combining MRI modalities provided information on the tissue functionality and water content. T1-w was efficient for anatomical discrimination and T2-w highlighted phenomena associated with host-pathogens interactions such as reaction zones. Interestingly, the T2-w signal dropped by approx. -60% between *functional* and *non-functional* tissues but increased by +110% between *non-functional* and *reaction zones*.

X-rays CT, on the other hand, was particularly efficient in detecting more advanced stages of wood deterioration characterized by a loss in structural integrity and highlighted by a 56% drop in X-ray absorbance between *degraded* and *white rot* tissues.

Multimodal imaging, together with the 4D registration step and machine learning to extract information, proved its efficacy: combining MRI and X-ray CT significantly increased the quality of tissue segmentation. All possible imaging combinations were finally compared for their efficiency, and it is now possible to select the modality(ies) best suited to specific needs. For example, combining T1-w, T2-w, and X-ray was optimal for *intact* and *degraded* tissues detection, but T2-w alone proved also efficient in case only one imaging modality is possible. For *white rot* detection, combining T1-w and X-ray, or using X-ray alone were the best options.

Monitoring wood degradation using X-ray tomography or MRI was previously tested in other species, mostly on blocks or planks, and using a single imaging technique (20-22). In grapevine, CT scan allowed visualizing the graft union (23), studying xylem refilling (24) and tyloses-occluded vessels (25), or quantifying starch in stems (26). It was also tested on leaves to investigate the origin of GTD foliar symptoms, suggesting that symptoms might be elicited from the trunk (4). X-ray CT and MRI were successfully combined to collect anatomical and functional information and investigate *in vivo* flows in stems (17). These techniques were recently tested for GTDs detection (19), but were applied separately and on different wood samples, preventing the possibility of combining modalities and thus limiting their effectiveness. Here we collected multimodal 3D data on whole trunks of aged plants and developed a pipeline for automatic analysis. Although vines were cut up to gather data to train and evaluate the classifier, this approach is now feasible without harming the

plants (Fig. 1). It opens several exciting prospects for GTD diagnosis and potential applications to other plants or complex diseases difficult to detect so far.

GTD indicators based on internal tissue degradation rather than external foliar symptoms

New light was shed on classical monitoring studies when we compared foliar symptom histories with internal degradations. While previous reports showed necrosis volumes could be linked to the probability of esca leaf symptoms occurrence and white rot volumes to apoplectic forms (6-8, 15), only weak correlations between tainted or necrotic tissue contents and foliar symptoms were generally observed (5, 27). In most studies, plants are considered "*healthy*" if not expressing any foliar symptoms for one or two years only. Our results confirmed that the appearance of foliar symptoms in a given year are not linked to the volume of internal wood degradations, and that foliar symptoms are not reliable markers of the plant's actual health status in the GTD context.

Here we considered that the internal tissue composition (*intact*, *degraded*, *white rot*) better reflects the severity of the disease affecting the vines and their actual condition.

It seemed particularly relevant for *asymptomatic* vines: half of them, harboring large volumes of unhealthy tissues, would have been erroneously categorized as "*healthy*" plants using the foliar symptom proxy. Indeed, *asymptomatic* vines could have reached advanced stages of GTDs while *symptomatic* ones could be relatively unharmed. In such cases, foliar symptoms-based diagnosis is not reliable and internal tissue content is the only reliable proxy of plant health. Necrotic and decay compartments are intuitively more stable indicators than foliage symptoms: once tissues have suffered irreversible alterations, they will remain obviously not functional.

An internal tissue-based model for accurate GTD diagnosis

A model based on the quality, quantity and position of internal tissues could be proposed for an accurate diagnosis. Different stages in trunk damages could be distinguished: "*Low*" damages would be characterized by low volumes of altered tissues; - "*moderate*" by significant *degraded* and decay contents but still a fair amount of peripheral *intact* tissues; and - "*critical*" by only very limited areas of *intact* tissues (Fig. 6). Assuming a non-destructive imaging detection, these stages could be evaluated directly in vineyards and permit a reliable diagnosis in living specimens. Based on cross-sections, a threshold value of 10% *white rot* in branches has been proposed as a predictor for the chronic form of Esca (8, 15). This value could be a proper threshold between the *low* and *moderate* phases defined here, while 20% *white rot* would be the limit toward the *critical* stage. However, *intact* tissues should also be considered: a minimum of 30% *intact* tissues located in the last centimeters of the trunk could be proposed as a threshold for *critical* status.

Here all necrotic tissues were regrouped in a single *degraded* class, but defining more tissue classes (e.g. different types of necrosis) could enable studying each wood disease separately.

Grapevine is a tortuous liana in which both the proportion and configuration of tissues are highly irregular along the trunk, and among plants. Thresholds for the transition from one stage to the other would probably need to be established according to the grapevine variety. Considering their vigor and capacity to produce new functional tissues every year, some varieties might be able to cope with large volumes of unhealthy tissues while maintaining sufficient physiological and hydraulic functions. Other

factors such as the environment, fungal pathogens and pruning mode might also influence the capacity of the plant to survive with only very limited *intact* tissues (1), and their impact could be measured using this novel non-destructive approach.

Predicting the course of diseases and assisting management strategies

The quantity and position of healthy and unhealthy tissues could be useful to predict the evolution of the plant sanitary status. According to *intact* tissue content, it would indeed be tempting to predict that an *asymptomatic* vine might soon develop symptoms, assuming its proximity to *neo-symptomatic* vines (Fig. 4.e). Considering *white rot* and *degraded* tissues, we could also guess that, among the *asymptomatic-resilient* vines, one was more likely to survive a few more years, whereas others were more likely to die in the next year or so. Additional and larger-scale data are required to confirm the effectiveness of these proxies for individual and accurate predictive diagnosis, but multimodal imaging already proved relevant for diagnosing the current status of the vines studied here.

White rot removal using a small chainsaw has been proposed to extend the life of seriously affected vines. This technique, called *curettage*, is under evaluation. It is particularly aggressive and applied "blindly", causing great damage to the plant. By giving access to the exact location and volume of sick tissues to be removed, our non-destructive approach could improve precision surgery by enabling low-damage access to the sick inner compartments. It will also permit *in vivo* evaluation of its long-term efficacy.

Finally, non-destructive and *in vivo* monitoring studies of internal tissue contents could help identify plants that require urgent intervention (i.e., local treatment, curettage, surveillance) or to prioritize replacements in plots, facilitating vineyards management.

CONCLUSION

By providing direct access to internal tissue degradations in living plants, non-destructive imaging and AI-based image analysis could provide new insights on complex diseases such as GTDs. A wide range of new, *in vivo*, and time-lapse studies now become accessible. For example, physiological responses to wounding and pathogen-linked infection could be monitored at tissue level to search for varietal tolerance. At the individual level, long-term surveillance of healthy, necrotic and decay tissues could fine-tune prediction models and allow the evaluation of potential curative solutions. The enigmatic origin of Esca foliar symptoms, and the influence of environmental factors on disease development could probably be investigated more efficiently than with traditional, destructive methods. Previous studies, based on a limited number of foliar symptom observations, might also have led to wrong interpretations, and could be revisited. If no alternative is possible, foliar symptoms should at least be considered with extreme caution, after multiple years of survey.

In medicine, imaging is often dedicated to single individuals, which is rarely the case for plants that are generally considered at the population level. In viticulture, however, plots are perennial, and each vine represents a long-term financial investment, especially in the Champagne region. Individual and non-destructive diagnosis is therefore of great interest for grapevine, whether to target a local treatment or to consider the replacement of specific individuals. Long-term and complex diseases are also generally more difficult to handle. Conceiving virtual digital twins of living vines would authorize monitoring complex diseases, modeling their evolution, and assessing the impact of novel solutions, at

different scales. Placing medical imaging at the bedside of grapevines offers great hopes and exciting perspectives and could help define next-generation management processes.

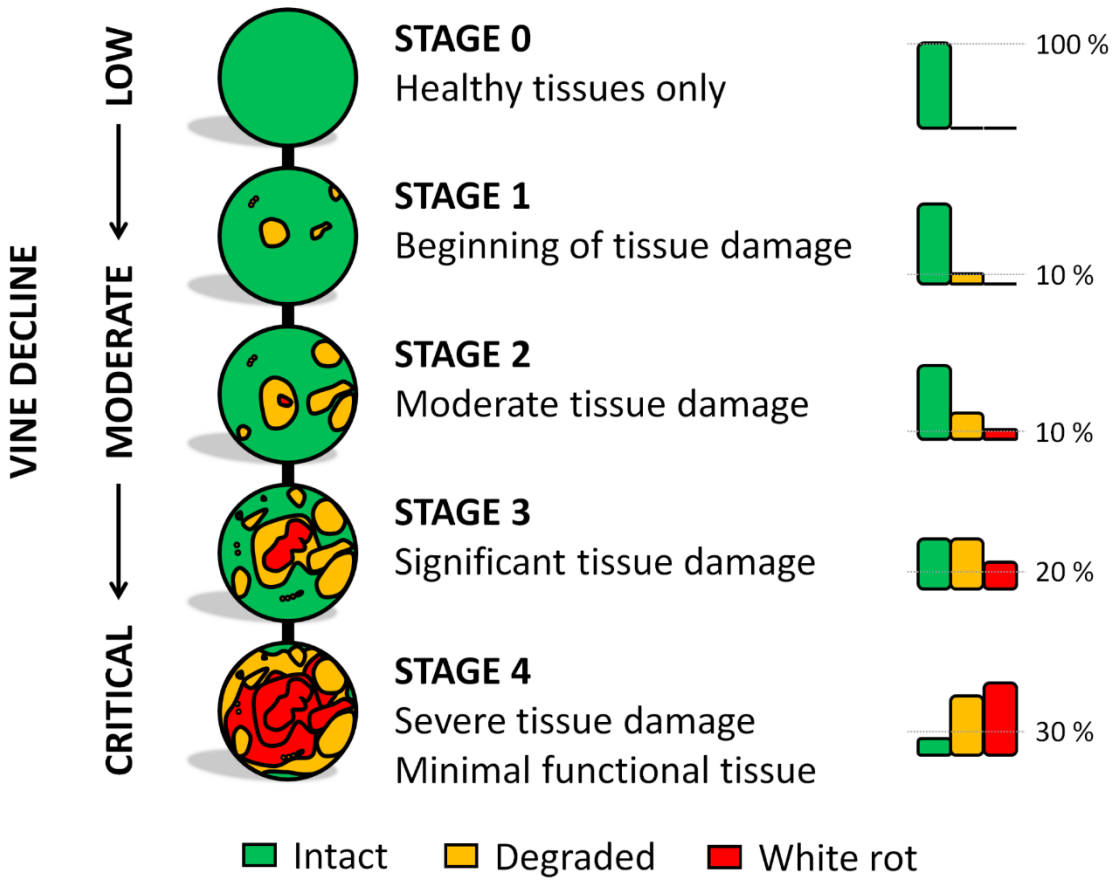

Figure 6: Model for GTD diagnosis based on the degree of trunk internal tissue degradation.

MATERIALS AND METHODS

Plants

A vineyard was planted in 1999 in Champagne, France, with *Vitis vinifera* L., cultivar Chardonnay rootstock 41B, and with a traditional Chablis pruning system. Each vine was monitored every year by CIVC for foliar symptom (FS) expression of grapevine trunk diseases (GTDs, including Esca, Black dead arm, *Botryosphaeria* and Eutypa diebacks). Observations were performed at different periods during the vegetative season to ensure the detection of different forms of GTDs, if present.

Based on FS observed in 2019, vines were considered *asymptomatic* (healthy) or *symptomatic* (sick).

Based on their whole FS history, vines were then sub-classified as:

1) *asymptomatic-always* if they never expressed any FS.
2) *asymptomatic-resilient* if they expressed FS in previous years but not in 2019.
3) *symptomatic-neo* if they expressed FS for the first time in 2019.
4) *symptomatic-apoplectic* if they died suddenly from typical apoplexy a few days before being collected.

For our study, vines showing different histories (three vines per subclass, 12 total, Fig. 3.a) were manually collected from the vineyard on the 19th of August 2019.

Branches and roots were cut out approx. 15 cm from the trunk, and plants were individually packed in sealed plastic bags to prevent drying.

Multimodal imaging acquisitions

Multimodal imaging acquisitions were performed on each vine individually, from rootstocks to the beginning of branches, by Magnetic Resonance Imaging (MRI) and X-ray Computed Tomography (CT).

MRI acquisitions were performed with Tridilogy SARL (http://www.tridilogy.com) and the help of radiologists from CRP/Groupe Vidi at the Clinique du Parc (Castelnau-le-Lez, France), using a Siemens Magnetom Aera 1,5 Tesla and a human head antenna. Three acquisition sequences, T1-weighted(-w), T2-w, and PD-w were performed on each specimen, respectively:

- 3D T1 Space TSE Sagittal (Thickness 0.6 mm, DFOV 56.5 x 35 cm, 320 images, NEx 1, EC 1, FA 120, TR 500, TE 4.1, AQM 256/256).
- 3D T2 Space Sagittal (Thickness 0.9mm, DFOV 57.4 x 35.5 cm, 160 images, NEx 2, EC 1, FA 160, TR 1100, TE 129, AQM 384/273).
- Axial Proton Density Fat Sat TSE Dixon (Ep 5mm, Sp 6.5, DFOV 57.2 x 38 cm, 40 images, NEx 1, EC 1, FA 160, TR 3370, TE 21, AQM 314/448).

X-ray CT acquisitions were performed at the Montpellier RIO Imaging platform (Montpellier, France, http://www.mri.cnrs.fr/en/) on an EasyTom 150kV microtomograph (RX Solution). 3D volumes were reconstructed using XAct software (RX solution) and resulted in approx. 2500 images per specimen at the resolution of 177 µm/voxel. Geometry, spot, and ring artifacts were corrected when necessary, using the default correction settings.

Plant slicing and photographic acquisition

After MRI and X-ray CT acquisitions, plants were individually placed in rigid PVC tubes, molded in a fast-setting polyurethane foam filler, and cut into 6 mm-thick cross-sections using a bandsaw (Fig. 1.3). Cutting thickness was approx. 1 mm. Marks were placed on tubes to ensure regular slicing, and three rigid plastic sticks with different diameters were molded together with vines to serve as landmarks for their realignment. Both faces of each cross-section were then photographed using a photography studio, artificial light, a tripod, a digital camera (Canon 500d), and a fixed-length lens (EF 50mm f/1.4 USM) to limit aberration and distortion.

Approximately 120 pictures per plant were collected and registered into a coherent 3D photographic volume based on landmarks.

Data preprocessing: 4D multi-modal registration

For each vine, 3D data from all modalities (MRI T1-w, T2-w and PD-w, X-ray CT, and 3D photographic volumes) were registered using Fijiyama (11) and combined into a single 4D-multimodal image (voxel size = 0.68 mm x 0.68 mm x 0.60 mm) (Fig. 1.4). To compensate for possible magnetic field biases, generally present at the edge of the fields during MRI acquisitions, we added checkpoints manually, facilitating the estimation of non-linear compensations during the 4D registration.

The registration accuracy was validated using manually placed landmarks (167 couples) distributed in the different modalities. Compared to MRI and X-ray CT modalities, the photographic volume presented a reduced number of images and light geometric distortions due to slicing irregularities. However, the alignment between photographs and other modalities resulted in an estimated average registration mismatch of 1.42 ± 0.98 mm (mean ± standard deviation). The alignment between photographs and other modalities was accurate enough to allow experts to perform a manual annotation of tissues directly on the 4D-multimodal images (see below).

Preliminary investigation of multi-modal signals

An initial signal study was carried out on eighty-four cross-sections randomly sampled from three vines.

Tissues were firstly classified in 6 different classes based on their visual appearance (Fig. 2.a): (i) "healthy-looking tissues" showing no sign of degradation; (ii) "black punctuations" corresponding to clogged vessels; (iii) "reaction zones" described earlier (12); (iv) "dry tissues" resulting from pruning injuries; (v) "degraded tissues" including several types of necrotic tissues; and (vi) "white rot".

Once considering X-ray CT and MRI images, experts were able to distinguish "intact functional" and "intact non functional" tissues among the "healthy-looking" class, resulting in a total of seven tissue classes (Fig. 2.a and 2.c). Moreover, some apparently "healthy-looking" tissues showed specific MRI hypo- or hyper-signals and were re-classified as "reaction zones" (Fig. 2.c). For these classes, an alteration of the wood aspect was not always visible by direct observation of the cross-sections.

Finally, multiple regions of interest (ROIs, 19,372 voxels total) were delineated by hand on the multimodal images and assigned to one of the seven tissue classes. For each selected voxel, values were gathered simultaneously from the four modalities (X-ray CT, T1-w, T2-w, and PD-w; 77,488 values total) using the registered multimodal images. The data were processed using R (v3.5.3) and the R-studio interface (v1.2.5001). Results are summarized in Fig. 2.d. The significance of differences observed between the seven tissue classes was tested within each modality using Tukey tests and a 95% family-wise confidence level.

Automatic tissues segmentation of the whole 3D datasets

For each plant, thirteen cross-sections were sampled and manually annotated to label the corresponding voxels. Five classes were defined as 1) background; 2) bark; and three tissue classes 3) intact tissues; 4) degraded tissues; and 5) white rot (Fig. 2.a). The annotation was performed using the Trainable segmentation plugin for Fiji (28), which was extended to process multi-channel 3D images (see code availability). As a result, a set of 81,454 annotated voxels distributed among the twelve 3D volumes was produced (Table S1).

We trained an algorithm to classify each voxel $P_i=(x,y,z)$ of the images (20 million voxels per specimen), attributing a class C_i among the five previously described (Fig 3.a). The classification was performed using the Fast Random Forest algorithm implemented in the Trainable Segmentation plugin given its performance when working with "small" training datasets (< 100.000 samples).

For each voxel, a feature vector X_i was built and then used by the classifier to predict the class $\hat{C}_i$ of the voxel P_i. Information on the voxel's local environment was gathered in the feature vector by applying various image processing operators (local mean value, variance, edge, etc.) to the initial images, and for each imaging modality. These operators were parameterized using a scale factor taking values from 1 to 64 voxels.

Evaluation of classifier performances

The classifier performances were evaluated using a k-fold cross-validation strategy. In each fold, the annotated voxels were split into a training set and a validation set. The train set, regrouping annotations from 10 plants, was used to train the classifier. The validation set, containing annotations from the two remaining plants, was used to assess the performances of the trained classifier. A global confusion matrix was then computed from all possible 66 folds (Table S3). From this matrix, global and class-specific accuracies, and F1-scores (considering both the test precision p and the recall r (29) were evaluated for each class and for all possible combinations of imaging modalities (Fig. 3.b and Table S2). F1-scores are generally considered as a better indicator of performance because they highlight more precisely under- and over-estimations of a specific class.

Tissue quantification and 3D volumes reconstruction

For further analysis, we only considered voxels corresponding to areas of interest, i.e., tissue classes *intact*, *degraded*, and *white rot*. The number and localization of these voxels were collected for tissue quantification and visualization. 3D views presented in Fig. 3.d and Fig. 5 were produced using isosurface extraction and volume rendering routines from VTK libraries (30).

Relative positioning of tissue classes along the vines

To compare the position of *intact*, *degraded*, and *white rot* tissues in different vines, we estimated the geodesic distance separating each voxel from a common reference area point located at the center of the trunk, twenty centimeters below trunk head. Using geodesic distances, we considered a region ranging from the last 20 cm of the trunk (defined as "position -20"), passing through the top of the trunk ("0"), to the first 5 cm of branches ("+5") (Fig. S2). This computation allowed the identification of voxel populations located within a same distance range while considering the tortuous shape of the trunks.

Simulation of performances at lower resolutions

To simulate an average portable imaging device's resolution, test images were built by image sub-sampling, resulting in voxel sizes ranging from 0.7 (original resolution) up to 10 mm. The corresponding annotated samples were converted accordingly, retaining the most represented label for each voxel volume. The classifier was then trained and tested on these low-resolution sample sets.

ACKNOWLEDGEMENTS

This work was supported by the French Ministry of Agriculture and Food, France AgriMer, the Comité National des Interprofessions des Vins à appellation d'origine et à indication géographique (CNIV), and the Institut Français de la Vigne et du Vin (IFV) within VITIMAGE and VITIMAGE-2024 projects (program Plan National Dépérissement du Vignoble); and by Agropolis fondation-APLIM Etendard project (contract 1504-005).

Imaging acquisitions were performed at Tridilogy SARL / Groupe CRP, and at the MRI platform member of the national infrastructure France-BioImaging supported by the French National Research Agency «Investments for the Future» (ANR-10-INBS-04), and of the Labex CEMEB (ANR-10-LABX-0004) and NUMEV (ANR-10-LABX-0020). The funders had no role in study design, data collection and analysis, decision to publish, or preparation of the manuscript.

Authors warmly thank Stéphane Bottalico and Renaud Lebrun (CNRS) for technical assistance.

AUTHOR CONTRIBUTION

Romain Fernandez: Methodology, Software, Investigation, Formal analysis, Visualization, Writing. **Loïc Le Cunff:** Conceptualization, Methodology, Investigation, Writing. **Samuel Mérigeaud:** Conceptualization, Methodology, Investigation, Data Curation. **Jean-Luc Verdeil:** Conceptualization, Methodology, Investigation, Writing. **Julie Perry:** Resources, Investigation. **Philippe Larignon:** Investigation, Data Curation, Writing. **Anne-Sophie Spilmont:** Conceptualization, Writing. **Philippe Chatelet:** Investigation, Writing. **Maïda Cardoso:** Conceptualization, Writing. **Christophe Goze-Bac:** Conceptualization, Writing. **Cédric Moisy:** Conceptualization, Methodology, Investigation, Formal analysis, Visualization, Funding acquisition, Supervision, Writing.

DATA AND CODE AVAILABILITY

The datasets generated and analyzed during the current study are available from the corresponding author upon reasonable request.

The extension of the Trainable Segmentation plugin is open-source, and available as a fork of Trainable Segmentation on GitHub: https://github.com/Rocsg/Trainable_Segmentation/tree/Hyperweka.

REFERENCES

1. Claverie M, Notaro M, Fontaine F, Wery J. Current knowledge on Grapevine Trunk Diseases with complex etiology: a systemic approach. Phytopathologia Mediterranea. 2020;59(1):29-53.
2. Fontaine F, Gramaje D, Armengol J, Smart R, Nagy ZA, Borgo M, et al. Grapevine trunk diseases. A review. 2016:24.
3. Guerin-Dubrana L, Fontaine F, Mugnai L. Grapevine trunk disease in European and Mediterranean vineyards: occurrence, distribution and associated disease-affecting cultural factors. Phytopathologia Mediterranea. 2019;58(1).
4. Bortolami G, Gambetta GA, Delzon S, Lamarque LJ, Pouzoulet J, Badel E, et al. Exploring the Hydraulic Failure Hypothesis of Esca Leaf Symptom Formation. Plant Physiol. 2019.
5. Mugnai L, Graniti A, Surico G. Esca (Black Measles) and Brown Wood-Streaking: Two Old and Elusive Diseases of Grapevines. Plant Dis. 1999;83(5):404-18.
6. Lecomte P, Darrieutort G, Liminana J-M, Comont G, Muruamendiaraz A, Legorburu FJ, et al. New Insights into Esca of Grapevine: The Development of Foliar Symptoms and Their Association with Xylem Discoloration. Plant Disease. 2012;96:924-34.
7. Péros JP, Berger G, Jamaux-Despréaux I. Symptoms, Wood Lesions and Fungi Associated with Esca in Organic Vineyards in Languedoc-Roussillon (France). Journal of Phytopathology. 2008;156(5):297-303.
8. Maher N, Piot J, Bastien S, Vallance J, Rey P, Guérin-Dubrana L. Wood necrosis in esca-affected vines: types, relationships and possible links with foliar symptom expression. OENO One. 2012;46(1).
9. Reis P, Pierron R, Larignon P, Lecomte P, Abou-Mansour E, Farine S, et al. Vitis Methods to Understand and Develop Strategies for Diagnosis and Sustainable Control of Grapevine Trunk Diseases. Phytopathology. 2019;109(6):916-31.
10. Laubenbacher R, Sluka JP, Glazier JA. Using digital twins in viral infection. Science. 2021;371(6534):1105-6.
11. Fernandez R, Moisy C. Fijiyama: a registration tool for 3D multimodal time-lapse imaging. Bioinformatics. 2021;37(10):1482-4.
12. Pearce RB. Decay development and its restriction in trees. Journal of Arboriculture. 2000;26(1):1-10.
13. Witten IH, Frank E, Hall MA, Pal CJ. Data Mining, Fourth Edition: Practical Machine Learning Tools and Techniques: Morgan Kaufmann Publishers Inc.; 2016.
14. Gramaje D, Urbez-Torres JR, Sosnowski MR. Managing Grapevine Trunk Diseases With Respect to Etiology and Epidemiology: Current Strategies and Future Prospects. Plant Disease. 2018;102(1):12-39.
15. Ouadi L, Bruez E, Bastien S, Vallance J, Lecomte P, Domec JC, et al. Ecophysiological impacts of Esca, a devastating grapevine trunk disease, on Vitis vinifera L. PLoS One. 2019;14(9):e0222586.
16. Mondello V, Songy A, Battiston E, Pinto C, Coppin C, Trotel-Aziz P, et al. Grapevine Trunk Diseases: A Review of Fifteen Years of Trials for Their Control with Chemicals and Biocontrol Agents. Plant Dis. 2018;102(7):1189-217.
17. Bouda M, Windt CW, McElrone AJ, Brodersen CR. In vivo pressure gradient heterogeneity increases flow contribution of small diameter vessels in grapevine. Nature Communications. 2019;10(1).
18. Van As H, van Duynhoven J. MRI of plants and foods. J Magn Reson. 2013;229:25-34.
19. Vaz AT, Del Frari G, Chagas R, Ferreira A, Oliveira H, Boavida Ferreira R. Precise nondestructive location of defective woody tissue in grapevines affected by wood diseases. Phytopathologia Mediterranea. 2020;59(3):441-51.
20. Hervé V, Mothe F, Freyburger C, Gelhaye E, Frey-Klett P. Density mapping of decaying wood using X-ray computed tomography. International Biodeterioration & Biodegradation. 2014;86:358-63.
21. Hamada J, Pétrissans A, Mothe F, Ruelle J, Pétrissans M, Gérardin P. Variations in the natural density of European oak wood affect thermal degradation during thermal modification. Annals of Forest Science. 2016;73(2):277-86.

22. Li W, Van den Bulcke J, De Windt I, Defoirdt N, Dhaene J, Dierick M, et al. Relating MOE decrease and mass loss due to fungal decay in plywood and MDF using resonalyser and X-ray CT scanning. International Biodeterioration & Biodegradation. 2016;110:113-20.
23. Milien M, Renault-Spilmont A-S, Cookson SJ, Sarrazin A, Verdeil J-L. Visualization of the 3D structure of the graft union of grapevine using X-ray tomography. Scientia Horticulturae. 2012;144:130-40.
24. Brodersen CR, Knipfer T, McElrone AJ. In vivo visualization of the final stages of xylem vessel refilling in grapevine (Vitis vinifera) stems. New Phytologist. 2018;217(1):117-26.
25. Czemmel S, Galarneau ER, Travadon R, McElrone AJ, Cramer GR, Baumgartner K. Genes Expressed in Grapevine Leaves Reveal Latent Wood Infection by the Fungal Pathogen Neofusicoccum parvum. PLOS ONE. 2015;10(3):e0121828.
26. Earles JM, Knipfer T, Tixier A, Orozco J, Reyes C, Zwieniecki MA, et al. In vivo quantification of plant starch reserves at micrometer resolution using X-ray microCT imaging and machine learning. New Phytol. 2018.
27. Calzarano F, Di Marco S. Wood discoloration and decay in grapevines with esca proper and their relationship with foliar symptoms. Phytopathologia Mediterranea. 2007;46(1):96-101.
28. Arganda-Carreras I, Kaynig V, Rueden C, Eliceiri KW, Schindelin J, Cardona A, et al. Trainable Weka Segmentation: a machine learning tool for microscopy pixel classification. Bioinformatics. 2017;33(15):2424-6.
29. Chinchor N, editor Muc-4 evaluation metrics. Proceedings of the 4th conference on Message understanding; 1992 June 1992.
30. Schroeder WJ, Martin KM. 30 - The Visualization Toolkit. In: Hansen CD, Johnson CR, editors. Visualization Handbook. Burlington: Butterworth-Heinemann; 2005. p. 593-614.

SUPPORTING INFORMATION

The following Supporting Information is available for this article:

	Classes						
Vine #	**Background**	**Intact tissues**	**Degraded tissues**	**White rot**	**Bark**	**Total samples**	**%**
01	683	3,749	2,699	155	560	**7,846**	*9.6*
02	781	3,079	2,490	337	599	**7,286**	*8.9*
03	252	2,231	2,106	49	528	**5,166**	*6.3*
04	538	2,290	3,155	1,450	550	**7,983**	*9.8*
05	135	2,013	2,690	2,681	192	**7,711**	*9.5*
06	272	2,168	2,821	1,250	301	**6,812**	*8.4*
07	317	2,743	2,343	1,169	451	**7,023**	*8.6*
08	461	2,179	2,247	665	319	**5,871**	*7.2*
09	288	2,868	1,500	479	559	**5,694**	*7.0*
10	403	2,154	2,578	2,167	180	**7,482**	*9.2*
11	192	2,004	2,755	894	358	**6,203**	*7.6*
12	274	1,123	2,733	2,009	238	**6,377**	*7.8*
Total	**4,596**	**28,601**	**3,0117**	**13,305**	**4,835**	**81,454**	*100*
%	*5.6*	*35.1*	*37.0*	*16.3*	*5.9*	*100*	

Table S1 Number of annotated samples available for classifier training and evaluation
Distribution among tissue classes and vines.

Table S2 Evaluation of classifier performances
Global and class accuracies (Acc), precision (Prec), recall (Rec) and F1-scores (F1) percentages. Mean (bold) and standard deviation (*italic*) were collected by training on ten vines and evaluating on the last two. Different combinations of imaging modalities were tested: MRI PD-w, T1-w, and T2-w; and X-ray CT (XR).

Mean *Std*	Imaging modalities considered				Global	Background				Intact				Degraded				White rot				Bark			
					Acc	Acc	Prec	Rec	F1	Acc	Prec	Rec	F1	Acc	Prec	Rec	F1	Acc	Prec	Rec	F1	Acc	Prec	Rec	F1
MRI only	PD				64.1	92.8	44.8	52.2	48.2	86.3	82.1	76.9	79.4	69.8	59.5	67.6	63.3	85.4	55.0	46.2	50.2	93.9	50.3	38.4	43.5
					8.7	*2.9*	*19.2*	*15.4*	*17.1*	*5.8*	*8.6*	*18.0*	*11.6*	*7.4*	*9.7*	*5.8*	*7.2*	*5.3*	*18.8*	*18.6*	*18.7*	*1.6*	*18.3*	*12.7*	*15.0*
		T1			76.4	95.0	68.3	79.9	73.7	91.4	84.9	90.8	87.8	80.5	74.7	72.7	73.7	89.7	70.9	61.9	66.1	96.3	71.0	63.9	67.2
					9.8	*5.5*	*25.9*	*8.0*	*12.2*	*3.1*	*8.4*	*8.8*	*8.6*	*6.6*	*9.1*	*7.9*	*8.4*	*6.0*	*13.5*	*21.0*	*16.4*	*1.5*	*16.7*	*12.7*	*14.4*
			T2		73.2	93.5	41.7	37.9	39.7	94.1	89.7	94.0	91.8	75.3	66.0	73.2	69.4	87.8	63.1	46.4	53.5	95.8	66.6	56.6	61.2
					5.5	*1.5*	*14.8*	*15.7*	*15.2*	*2.1*	*4.4*	*6.1*	*5.1*	*5.7*	*7.8*	*5.6*	*6.5*	*5.7*	*14.9*	*20.4*	*17.2*	*1.1*	*15.1*	*13.3*	*14.1*
		T1	T2		80.2	94.8	66.6	78.5	72.1	95.5	91.9	95.8	93.8	83.8	77.8	80.3	79.0	89.6	72.7	57.3	64.1	96.7	77.0	64.8	70.4
					7.6	*5.7*	*25.2*	*8.9*	*13.1*	*1.6*	*2.8*	*4.1*	*3.3*	*4.5*	*7.7*	*5.2*	*6.2*	*6.2*	*12.3*	*21.6*	*15.6*	*1.5*	*14.7*	*12.0*	*13.2*
	PD	T1			75.1	94.9	68.4	77.3	72.5	91.6	85.4	91.1	88.2	78.9	70.7	74.0	72.3	88.8	70.8	54.6	61.6	96.0	70.5	55.4	62.0
					8.1	*5.4*	*26.0*	*8.5*	*12.8*	*2.2*	*7.4*	*6.2*	*6.7*	*5.2*	*7.8*	*5.8*	*6.7*	*6.0*	*13.8*	*20.5*	*16.5*	*1.2*	*18.4*	*16.3*	*17.3*
	PD		T2		73.7	93.5	52.4	50.1	51.2	93.7	89.3	93.8	91.5	76.3	66.9	74.0	70.3	87.8	65.8	46.1	54.2	96.0	70.6	58.0	63.7
					5.7	*2.7*	*22.6*	*17.2*	*19.6*	*2.3*	*5.0*	*6.3*	*5.6*	*5.0*	*8.6*	*7.2*	*7.8*	*5.5*	*16.4*	*18.4*	*17.4*	*1.0*	*14.9*	*14.6*	*14.7*
	PD	T1	T2		78.8	94.6	66.3	78.1	71.7	95.2	91.0	96.1	93.5	82.4	75.1	79.5	77.2	88.8	72.7	50.2	59.4	96.7	76.3	64.2	69.8
					7.4	*5.9*	*25.3*	*8.8*	*13.1*	*1.9*	*3.8*	*4.0*	*3.9*	*4.5*	*7.9*	*5.9*	*6.7*	*6.1*	*11.8*	*20.4*	*14.9*	*1.1*	*14.5*	*12.7*	*13.5*
XR only				XR	85.6	99.7	97.0	97.4	97.2	88.8	83.2	86.2	84.7	87.0	83.8	80.9	82.3	98.1	91.8	93.4	92.6	97.7	79.6	83.9	81.7
					2.7	*0.2*	*4.0*	*2.3*	*2.9*	*2.6*	*6.7*	*5.2*	*5.9*	*2.6*	*5.9*	*6.3*	*6.1*	*0.5*	*9.2*	*2.9*	*4.4*	*1.2*	*9.1*	*6.6*	*7.7*
MRI and XR	PD			XR	86.9	99.7	97.5	97.3	97.4	89.9	85.4	86.2	85.8	88.0	84.3	83.6	84.0	98.1	91.8	93.6	92.7	98.0	82.7	84.9	83.8
					2.5	*0.2*	*2.6*	*2.3*	*2.5*	*2.6*	*7.6*	*6.2*	*6.8*	*2.4*	*5.6*	*6.6*	*6.0*	*0.5*	*9.1*	*2.8*	*4.3*	*0.7*	*7.2*	*6.4*	*6.8*
		T1		XR	88.8	99.6	96.1	97.3	96.7	91.9	86.4	90.8	88.5	89.7	87.9	84.3	86.1	98.2	92.5	93.4	93.0	98.3	86.1	86.1	86.1
					2.8	*0.3*	*5.4*	*2.2*	*3.1*	*2.4*	*7.0*	*8.5*	*7.7*	*2.3*	*5.2*	*5.5*	*5.4*	*0.7*	*9.3*	*3.5*	*5.1*	*0.8*	*8.5*	*6.8*	*7.6*
			T2	XR	92.0	99.7	97.9	97.2	97.5	95.1	91.7	94.7	93.2	92.5	90.8	88.7	89.7	98.2	92.2	93.4	92.8	98.5	87.5	86.1	86.8
					1.5	*0.2*	*2.4*	*2.2*	*2.3*	*1.7*	*3.5*	*5.1*	*4.1*	*1.5*	*3.6*	*3.5*	*3.5*	*0.4*	*9.2*	*3.0*	*4.5*	*0.6*	*6.5*	*5.6*	*6.0*
	PD	T1		XR	88.5	99.6	96.2	97.3	96.7	91.6	86.2	90.4	88.2	89.4	87.2	84.2	85.7	98.1	92.5	92.9	92.7	98.3	86.6	85.2	85.9
					2.1	*0.5*	*6.6*	*2.1*	*3.2*	*1.9*	*7.2*	*5.9*	*6.5*	*1.8*	*4.6*	*6.1*	*5.3*	*0.9*	*9.3*	*4.2*	*5.8*	*0.7*	*8.5*	*6.0*	*7.0*
	PD		T2	XR	91.3	99.7	97.9	97.0	97.4	94.5	90.8	94.2	92.5	91.9	90.2	87.6	88.9	98.1	92.1	93.0	92.6	98.4	87.7	85.4	86.6
					1.6	*0.2*	*2.1*	*2.2*	*2.1*	*1.9*	*4.3*	*5.8*	*4.9*	*1.6*	*4.3*	*5.0*	*4.6*	*0.5*	*9.2*	*3.1*	*4.6*	*0.5*	*7.0*	*5.9*	*6.4*
		T1	T2	XR	92.1	99.3	91.5	96.9	94.2	95.6	92.3	95.6	93.9	93.0	91.5	89.5	90.5	97.7	92.3	91.4	91.9	98.4	87.3	86.0	86.7
					1.8	*0.9*	*15.3*	*2.1*	*3.7*	*1.6*	*2.8*	*4.2*	*3.4*	*1.5*	*3.6*	*2.8*	*3.2*	*1.2*	*9.2*	*4.4*	*5.9*	*0.6*	*7.5*	*6.0*	*6.6*
	PD	T1	T2	XR	91.6	99.2	90.5	96.8	93.5	95.3	91.4	95.9	93.6	92.7	91.5	88.6	90.0	97.5	92.3	90.5	91.4	98.4	87.3	85.5	86.4
					2.0	*1.1*	*17.4*	*2.1*	*3.7*	*1.7*	*3.4*	*4.1*	*3.7*	*1.5*	*3.8*	*3.7*	*3.8*	*1.5*	*9.2*	*5.3*	*6.8*	*0.7*	*8.7*	*5.8*	*6.9*

		REAL classes					
	Sample #	Back-ground	Intact	Degraded	White rot	Bark	%
PREDICTED	Background	**48,824**	4	32	3,818	894	*6.0*
	Intact	0	**300,293**	24,096	0	1,065	*36.3*
	Degraded	31	13,611	**296,931**	9,085	5,276	*36.3*
	White rot	652	3	6,26	**132,996**	455	*15.7*
	Bark	1,049	700	3,968	456	**45,495**	*5.8*
	%	*5.6*	*35.1*	*37.0*	*16.3*	*5.9*	

Table S3 Evaluation of the classifier performance: sum of confusion matrices
Considering the 66 folds of the cross-validation.

	Tissue classes		
Imaging modalities	Intact	Degraded	White rot
X-ray	**129,4**	**104,5**	**46,0**
	21,3	*24,6*	*14,1*
T1-w	**110,2**	**47,1**	**29,7**
	40,0	*42,6*	*19,7*
T2-w	**68,9**	**9,4**	**2,2**
	46,1	*20,4*	*3,0*
PD-w	**41,8**	**12,0**	**4,3**
	37,2	*17,4*	*6,8*

Table S4 Multimodal signal values corresponding to the three main tissue classes
Means (in bold) and standard deviations (italic) (values in 8-bits) collected on the whole dataset (after automatic classification, 46.2 million voxels total).

			Tissue content cm^3 (%)		
Vine #	**Phenotype**		**Intact**	**Degraded**	**White rot**
01	AS-A	ASymptomatic Always	687 (2,0)	302 (29,9)	21 (68,0)
02	AS-A	ASymptomatic Always	571 (4,2)	278 (31,3)	38 (64,3)
03	AS-A	ASymptomatic Always	663 (1,7)	336 (33,0)	18 (65,1)
04	SY-N	Symptomatic Neo	722 (9,5)	395 (31,9)	118 (58,4)
05	SY-N	Symptomatic Neo	426 (7,9)	450 (47,2)	76 (44,7)
06	SY-N	Symptomatic Neo	559 (9,1)	334 (33,9)	90 (56,8)
07	AS-R	ASymptomatic Resilient	278 (19,2)	623 (55,8)	215 (24,9)
08	AS-R	ASymptomatic Resilient	357 (23,6)	551 (46,3)	281 (30,0)
09	AS-R	ASymptomatic Resilient	421 (10,8)	368 (41,5)	96 (47,5)
10	SY-A	SYmptomatic Apoplectic	333 (20,8)	436 (44,9)	202 (34,2)
11	SY-A	SYmptomatic Apoplectic	425 (12,2)	685 (54,1)	155 (33,5)
12	SY-A	SYmptomatic Apoplectic	252 (17,5)	565 (57,0)	174 (25,4)

Table S5 Tissue contents per vine

Contents measured for each individual vine from the automatically segmented 3D datasets. Data were collected in the region ranging from the upper last 20 cm of the trunks to the first 5 cm of the branches. Results are expressed as volume (cm3) and percentages.

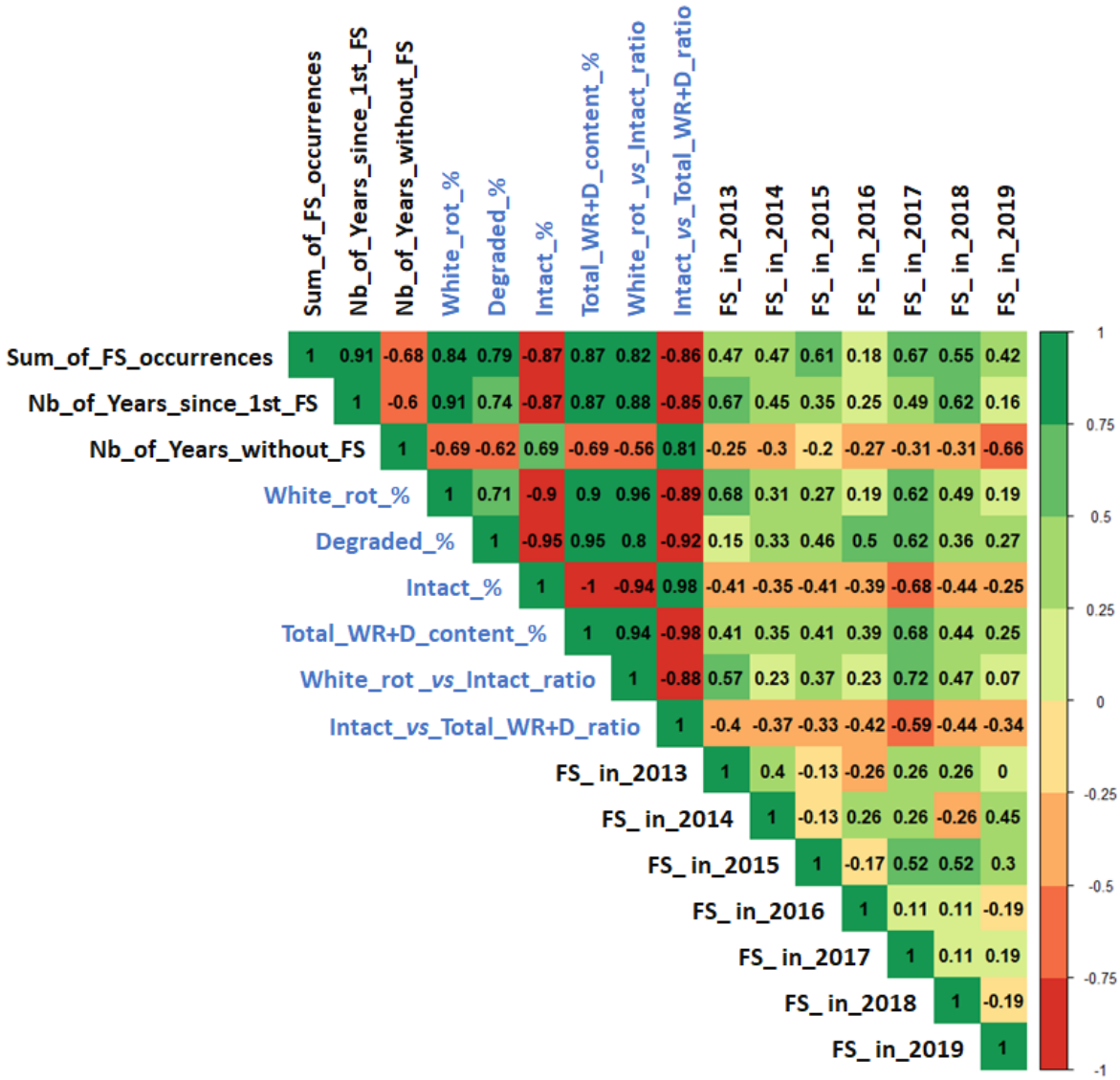

Table S6 Correlogram

Chart of correlation statistics between “internal” (blue text) and “external” (black text) proxies for GTD status diagnosis. FS= foliar symptom; Nb= number; D= degraded tissues; WR= white rot.

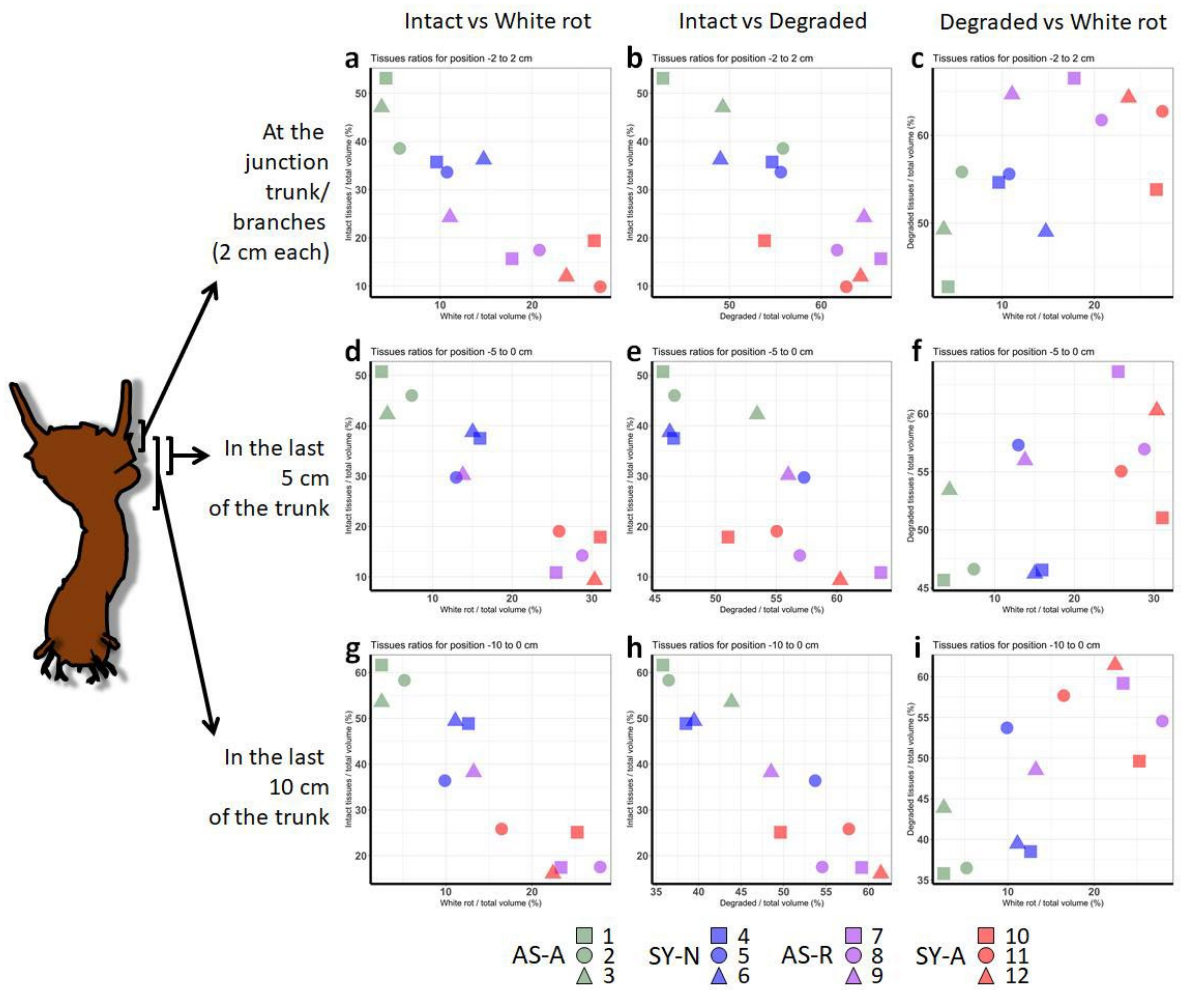

Fig. S1 Detailed comparison of vines for intact, degraded, and white rot contents considering different positions along the vine trunk

AS-A= asymptomatic-always; SY-N= symptomatic-neo; AS-R= asymptomatic-resilient; SY-A= symptomatic-apoplectic.

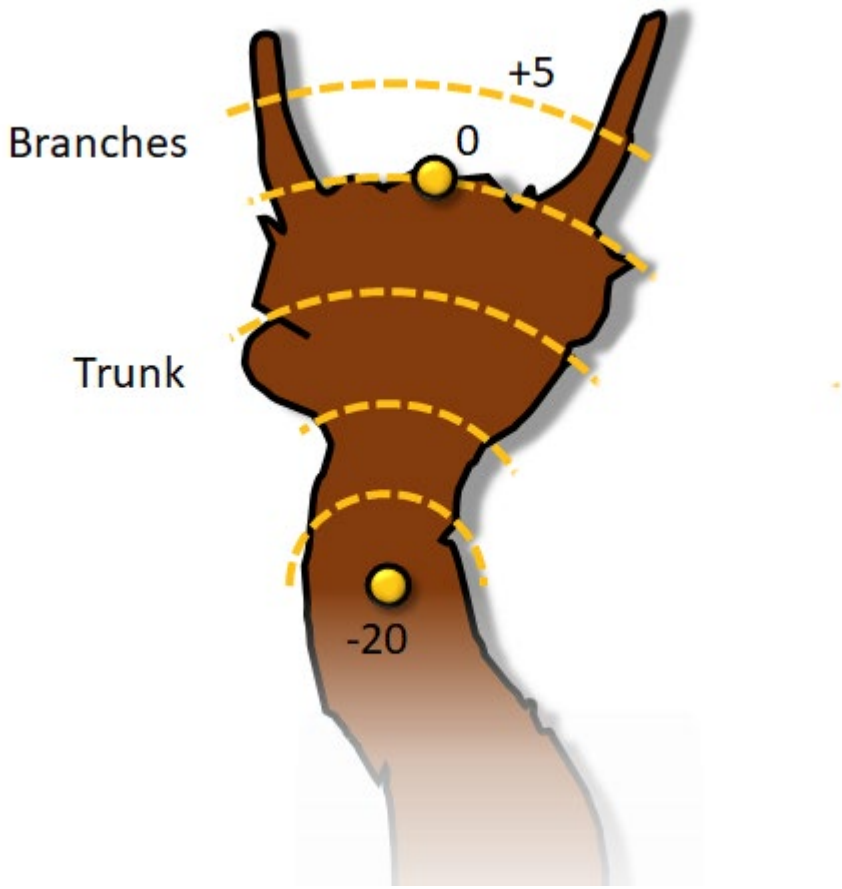

Fig. S2 Vine trunk geodesic distance estimation
Geodesic distances were estimated from the center of the trunk and using the top of the trunk as a reference (point “0”).